

VIRTUAL ELEMENT FORMULATION FOR PHASE-FIELD MODELING OF DUCTILE FRACTURE

Fadi Aldakheel, Blaž Hudobivnik, & Peter Wriggers*

Institute of Continuum Mechanics, Leibniz Universität Hannover, Appelstrasse 11, 30167 Hannover, Germany

*Address all correspondence to: Fadi Aldakheel, Institute of Continuum Mechanics, Leibniz Universität Hannover, Appelstrasse 11, 30167 Hannover, Germany, E-mail: aldakheel@ikm.uni-hannover.de

Original Manuscript Submitted: 6/4/2018; Final Draft Received: 10/8/2018

An efficient low-order virtual element method (VEM) for the phase-field modeling of ductile fracture is outlined within this work. The recently developed VEM is a competitive discretization scheme for meshes with highly irregular shaped elements. The phase-field approach is a very powerful technique to simulate complex crack phenomena in multi-physical environments. The formulation in this contribution is based on a minimization of a pseudo-potential density functional for the coupled problem undergoing large strains. The main aspect of development is the extension toward the virtual element formulation due to its flexibility in dealing with complex shapes and arbitrary number of nodes. Two numerical examples illustrate the efficiency, accuracy, and convergence properties of the proposed method.

KEY WORDS: *virtual element method (VEM), phase-field modeling, ductile fracture, elastic-viscoplastic solids*

1. INTRODUCTION

The virtual element method (VEM) has been developed over the last decade and applied to various problems in solid mechanics. It is a generalization of the finite element method (FEM) (Bathe, 1996; Wriggers, 2008; Zienkiewicz et al., 2005), which has been inspired from modern mimetic finite difference schemes in Brezzi et al. (2009). VEM allows exploration of features such as flexibility with regard to mesh generation and choice of element shapes, e.g., the use of very general polygonal and polyhedral meshes. In this regard, a stabilization procedure is required in the virtual element method, as described in Cangiani et al. (2015) for linear Poisson problems. Up until now, applications of virtual elements have been devoted to linear elastic deformations in Artioli et al. (2017) and Gain et al. (2014), contact problems in Wriggers et al. (2016), finite elasto-plastic deformations in Hudobivnik et al. (2019) and Wriggers and Hudobivnik (2017), anisotropic materials at finite strains in Wriggers et al. (2018a,b), small strain isotropic damage in Bellis et al. (2018), inelastic solids in Taylor and Artioli (2018) and hyperelastic materials at finite deformations in Chi et al. (2017) and Wriggers et al. (2017). Recently, Aldakheel et al. (2018a) propose an efficient virtual element scheme for the phase-field modeling of brittle fracture at small strains. This paper extends VEM towards finite deformations ductile fracture using the phase-field approach.

The development of a virtual element methodology for solving fracture-mechanics problems numerically includes a projection step and a stabilization step. In the projection step, the deformation map $\boldsymbol{\varphi}$ and the fracture phase-field d which appear in the pseudo-potential density functional are replaced by their projection: $\boldsymbol{\varphi}_{\Pi}$ and d_{Π} onto a polynomial space. This results in a rank-deficient structure; therefore, it is necessary to add a stabilization term to the formulation (Beirão Da Veiga et al., 2013a,b; Chi et al., 2017), where in the latter the scalar stabilization parameter of the linear case was replaced by one that depends on the fourth-order elasticity tensor. A new stabilization technique for VEM was recently developed in Wriggers et al. (2017) who use a technique that was first described in Nadler and Rubin (2003), generalized in Boerner et al. (2007), and simplified in Krysl (2015a) in the context of hexahedral finite elements. The essence of the method is the addition of the pseudo-energy density function $W(\nabla \boldsymbol{\varphi}_{\Pi}, d_{\Pi}, \nabla d_{\Pi}, \mathbf{h})$

to a density function $\widehat{W}(\nabla \boldsymbol{\varphi}, d, \nabla d, \mathbf{h})$ which is evaluated using full quadrature. For consistency the subtraction of a term involving $\widehat{W}(\nabla \boldsymbol{\varphi}_{\Pi}, d_{\Pi}, \nabla d_{\Pi}, \mathbf{h})$ as a function of the projected deformation map and the crack phase field is made. Here \mathbf{h} is the history field array for the plastic strain measures and the crack driving force. This history array is locally evaluated only once at the element level and used in all parts of the pseudo-energy density function.

In the presented work, we examine the efficiency of VEM for predicting ductile failure mechanisms in solids due to crack initiation and propagation. The modeling of crack formation can be achieved in a convenient way by continuum phase-field approaches to fracture, which are based on the regularization of sharp crack discontinuities. Phase-field modeling of fracture has been attracting considerable attention in recent years due to its capability of capturing complex crack patterns in various problems in solid mechanics. Many efforts have been focused on the regularized modeling of Griffith-type brittle fracture in elastic solids. In this regard, Miehe et al. (2010) proposed a phase-field approach to fracture with a local irreversibility constraint on the crack phase-field. It incorporates regularized crack surface density functions as central constitutive objects, which is motivated in a descriptive format based on geometric considerations. Recent works on brittle fracture have been devoted to the dynamic case in Borden et al. (2012), cohesive fracture in Verhoosel and de Borst (2013), multiplicative decomposition of the deformation gradient into compressive-tensile parts in Hesch and Weinberg (2014), different choices of degradation functions in Kuhn et al. (2015), coupled thermo-mechanical and multi-physics problems at large strains in Dittmann et al. (2019) and Miehe et al. (2015b), to model fracture of arterial walls with an emphasis on aortic tissues in Gültekin et al. (2016), finite-deformation contact problems in Hesch et al. (2016), emphasis on a possible formula for the length scale estimation in Zhang et al. (2017), anisotropic material behavior at small and large deformations in Bleyer and Alessi (2018) and Teichtmeister et al. (2017), for the description of hydraulic fracturing in Ehlers and Luo (2017) and Heider and Markert (2017), to describe fatigue effects for brittle materials in Alessi et al. (2018b), to the modeling of fracture in polymeric hydrogels in Böger et al. (2017), for enhanced assumed strain shells at large deformations in Reinoso et al. (2017), and the virtual element method in Aldakheel et al. (2018a).

Extensions of these models toward the phase-field modeling of ductile fracture can be achieved by coupling of gradient damage mechanics with models of elasto-plasticity. In this regard, Duda et al. (2014) investigate a setting of brittle fracture in elastic-plastic solids. In Miehe et al. (2015a), the modeling of dynamic fracture in the logarithmic Lagrangian strain space has been presented with emphasis on the brittle to ductile transition in thermo-elastic-plastic solids. The model suggested in Ambati et al. (2015) uses a characteristic degradation function that couples damage to plasticity in a multiplicative format. Borden et al. (2016) proposes a mechanism for including a measure of stress triaxiality as a driving force for crack initiation and propagation. The coupling of gradient plasticity with gradient damage at finite strains is considered in Aldakheel (2016), Aldakheel et al. (2014), Dittmann et al. (2017, 2018a), and Miehe et al. (2016a,b,c, 2017) based on a rigorous variational principle. In Alessi et al. (2018a) a comparative study between different phase-field models of fracture coupled with plasticity is outlined. A coupled phase-field and plasticity modeling of geological materials is recently proposed by Aldakheel et al. (2017) and Choo and Sun (2018). Recently, Aldakheel et al. (2018b) extend the phase-field modeling of fracture toward porous finite plasticity to account for complex phenomena at the micro-scale, such as nucleation, growth, and coalescence of micro-voids, as well as the final rupture at the macro-scale.

A minimization of a pseudo-potential density functional for the phase-field modeling of ductile fracture is presented as a key goal of this work by using an efficient virtual element method. It is based on the definition of a pseudo-energy density per unit volume, that contains the sum of a degrading elastic-plastic part and a contribution due to fracture, in line with Aldakheel (2016) and Miehe et al. (2015a, 2016a). On the computational side, a robust and efficient monolithic scheme is employed in the numerical implementation to compute the unknowns (the deformation map and the crack phase-field) using the software tool ACEFEM (Korelc and Wriggers, 2016).

The paper is organized as follows: Section 2 outlines the governing equations for the phase-field approach to ductile fracture in elastic-plastic solids undergoing large deformations. The development of the virtual element method is formulated in Section 3. Finally, Section 4 presents numerical results that demonstrate the modeling capabilities of the proposed approach. The formulation performs extremely well in benchmark tests involving regular, distorted, and Voronoi meshes. For purpose of comparison, results of the standard finite element method (FEM) are also demonstrated.

2. GOVERNING EQUATIONS FOR PHASE-FIELD DUCTILE FRACTURE

This section outlines a theory of fracture in elastic-plastic solids at large deformations. It is based on a minimization of a pseudo-potential energy for the coupled problem. To this end, let $\Omega \in \mathcal{R}^\delta$ with $\delta = 2, 3$ be the reference configuration of a solid domain. The response of fracturing solid at material points $\mathbf{X} \in \Omega$ and time $t \in \mathcal{T} = [0, T]$ is described by the deformation map $\boldsymbol{\varphi}(\mathbf{X}, t)$ and the crack phase-field $d(\mathbf{X}, t)$ as

$$\boldsymbol{\varphi} : \begin{cases} \Omega \times \mathcal{T} \rightarrow \mathcal{R}^\delta \\ (\mathbf{X}, t) \mapsto \mathbf{x} = \boldsymbol{\varphi}(\mathbf{X}, t) = \mathbf{X} + \mathbf{u}(\mathbf{X}, t) \end{cases} \quad \text{and} \quad d : \begin{cases} \Omega \times \mathcal{T} \rightarrow [0, 1] \\ (\mathbf{X}, t) \mapsto d(\mathbf{X}, t) \end{cases} \quad \text{with} \quad \dot{d} \geq 0, \quad (1)$$

where \mathbf{x} is the position of a material point in the deformed configuration and $\mathbf{u}(\mathbf{X}, t)$ is the displacement field. The crack phase-field $d(\mathbf{X}, t) = 0$ and $d(\mathbf{X}, t) = 1$ refer to the unbroken and fully broken state of the material respectively, as visualized in Fig. 1. The material deformation gradient is defined by $\mathbf{F} := \nabla \boldsymbol{\varphi}_t(\mathbf{X}) = \text{Grad} \boldsymbol{\varphi}$ with the Jacobian $J := \det[\mathbf{F}] > 0$. The solid is loaded by prescribed deformations and external traction on the boundary, defined by time-dependent Dirichlet- and Neumann conditions

$$\boldsymbol{\varphi} = \bar{\boldsymbol{\varphi}}(\mathbf{X}, t) \text{ on } \partial\Omega_\varphi \quad \text{and} \quad \mathbf{P}\mathbf{N} = \bar{\mathbf{t}}(\mathbf{X}, t) \text{ on } \partial\Omega_t, \quad (2)$$

where \mathbf{N} is the outward unit normal vector on the surface $\partial\Omega = \partial\Omega_\varphi \cup \partial\Omega_t$ of the undeformed configuration. The first Piola-Kirchhoff stress tensor \mathbf{P} is the thermodynamic dual to \mathbf{F} . In finite strain plasticity, the deformation gradient is multiplicatively decomposed into an elastic and a plastic part as

$$\mathbf{F} = \mathbf{F}_e \mathbf{F}_p \quad \text{with} \quad J = J_e J_p = J_e = \det[\mathbf{F}_e] \quad \text{and} \quad J_p = \det[\mathbf{F}_p] = 1, \quad (3)$$

where the constraint of plastic incompressibility holds for the case of von Mises J_2 -plasticity. The elastic part of the right Cauchy-Green tensor $\mathbf{C} = \mathbf{F}^T \mathbf{F}$ can be computed as

$$\mathbf{C} = \mathbf{F}_p^T \mathbf{F}_e^T \mathbf{F}_e \mathbf{F}_p = \mathbf{F}_p^T \mathbf{C}_e \mathbf{F}_p \quad \text{yields} \quad \mathbf{C}_e = \mathbf{F}_p^{-T} \mathbf{C} \mathbf{F}_p^{-1}. \quad (4)$$

Furthermore, the elastic left Cauchy-Green tensor \mathbf{b}_e is defined as

$$\mathbf{b}_e = \mathbf{F}_e \mathbf{F}_e^T = \mathbf{F} \mathbf{C}_p^{-1} \mathbf{F}^T \quad \text{with} \quad \mathbf{C}_p = \mathbf{F}_p^T \mathbf{F}_p, \quad (5)$$

where \mathbf{C}_p is the plastic part of the right Cauchy-Green tensor. To account for phenomenological hardening/softening response, we define the equivalent plastic strain variable by the evolution equation

$$\dot{\alpha} = \dot{\gamma} \quad \text{with} \quad \dot{\alpha} \geq 0 \quad (6)$$

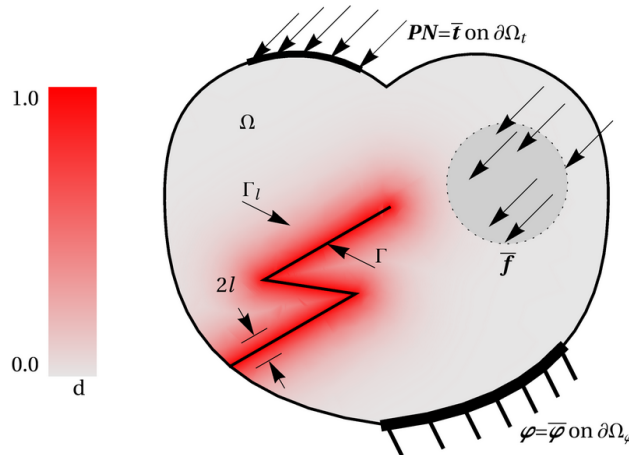


FIG. 1: Solid with a regularized crack and boundary conditions

as a local internal variable, where $\dot{\gamma} \geq 0$ is the plastic Lagrange multiplier. The hardening variable starts to evolve from the initial condition $\alpha(\mathbf{X}, 0) = 0$.

The solid Ω has to satisfy the equation of equilibrium as

$$\boxed{\text{Div } \mathbf{P} + \bar{\mathbf{f}} = \mathbf{0}}, \quad (7)$$

where dynamic effects are neglected and $\bar{\mathbf{f}}$ is the given body force.

For the phase-field problem, a sharp-crack surface topology $\Gamma \rightarrow \Gamma_l$ is regularized by the crack surface functional as outlined in Miehe et al. (2010, 2015a)

$$\Gamma_l(d) = \int_{\Omega} \gamma_l(d, \nabla d) dV \quad \text{with} \quad \gamma_l(d, \nabla d) = \frac{1}{2l} d^2 + \frac{l}{2} |\nabla d|^2, \quad (8)$$

based on the crack surface density function γ_l per unit volume of the solid and the fracture length scale parameter l that governs the regularization, as plotted in Fig. 1. To describe a purely geometric approach to phase-field fracture, the regularized crack phase-field d is obtained by a minimization principle of diffusive crack topology

$$d = \text{Arg}\{\inf_d \Gamma_l(d)\} \quad \text{with} \quad d = 1 \text{ on } \Gamma \subset \Omega, \quad (9)$$

yielding the Euler equation $d - l^2 \Delta d = 0$ in Ω along with the Neumann-type boundary condition $\nabla d \cdot \mathbf{N} = 0$ on $\partial\Omega$. Figure 2 demonstrates a numerical solution for Eq. (9) in two-dimensional setting using an efficient virtual element method (VEM). The $\Gamma_l(d)$ limit of the above variational principle gives for $l \rightarrow 0$ the sharp crack surface Γ , as depicted in Fig. 2(f) for the VE-shape specimen with a Voronoi mesh. Evolution of the regularized crack surface

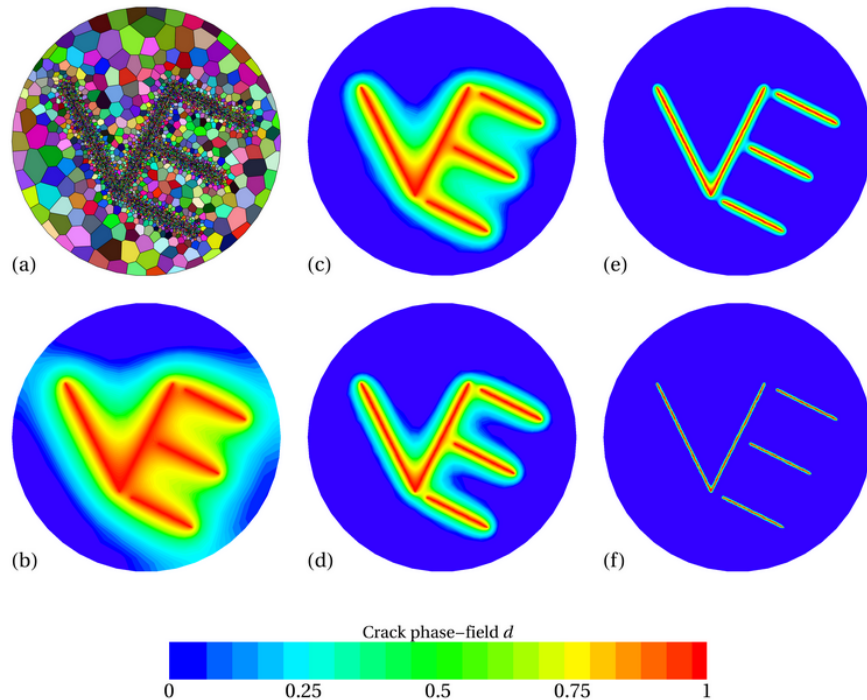


FIG. 2: A purely geometric approach to phase-field fracture based on virtual element method (VEM). (a) Geometry and discretization of the specimen using *Voronoi meshes*. (b)–(f) Solutions of the variational problem (9) for a circular specimen Ω with a given VE shape for the sharp crack Γ , prescribed by the Dirichlet condition $d = 1$ on $\Gamma \subset \Omega$ for different fracture length scales $l^b > l^c > l^d > l^e > l^f$.

functional (8) can be driven by the constitutive functions as outlined in Aldakheel et al. (2018b) and Miehe et al. (2015a), postulating a global evolution equation of regularized crack surface as

$$\frac{d}{dt}\Gamma_l(d) = \int_{\Omega} \delta_d \gamma_l(d, \nabla d) \dot{d} dV := \frac{1}{l} \int_{\Omega} [(1-d)\mathcal{H} - \eta_f \dot{d}] \dot{d} dV \geq 0, \quad (10)$$

where $\eta_f \geq 0$ is a material parameter that characterizes the artificial/numerical viscosity of the crack propagation. The crack driving force

$$\mathcal{H} = \max_{s \in [0, t]} D(\mathbf{X}, s) \geq 0, \quad (11)$$

is introduced as a *local history variable* that accounts for the irreversibility of the phase-field evolution by filtering out a maximum value of what is known as the crack driving state function D . Then the evolution statement (10) provides the local equation for the evolution of the crack phase field in the domain Ω along with its homogeneous Neumann boundary condition as

$$\boxed{\eta_f \dot{d} = (1-d)\mathcal{H} - [d - l^2 \Delta d] \quad \text{with} \quad \nabla d \cdot \mathbf{N} = 0 \quad \text{on} \quad \partial\Omega.} \quad (12)$$

The above-introduced variables will characterize the ductile failure response of a solid, based on the two global primary fields

$$\text{Global Primary Fields : } \mathfrak{U} := \{\boldsymbol{\varphi}, d\}, \quad (13)$$

the deformation map $\boldsymbol{\varphi}$, and the crack phase-field d . The constitutive approach to the phase-field modeling of ductile fracture focuses on the set

$$\text{Constitutive State Variables : } \mathfrak{C} := \{\mathbf{b}_e, \alpha, \mathcal{H}, d, \nabla d\}, \quad (14)$$

reflecting a combination of elasto-plasticity with a first-order gradient damage modeling. It is based on the definition of a pseudo-energy density per unit volume contains the sum

$$\boxed{W(\mathfrak{C}) = W_{elas}(\mathbf{b}_e, d) + W_{plas}(\alpha, d) + W_{frac}(\mathcal{H}, d, \nabla d)}, \quad (15)$$

of a degrading elastic W_{elas} and plastic energies W_{plas} and a contribution due to fracture W_{frac} , which contains the accumulated dissipative energy in line with Aldakheel (2016) and Miehe et al. (2016a). The elastic contribution is the neo-Hookean strain energy function for a homogeneous compressible isotropic elastic material

$$W_{elas}(\mathbf{b}_e, d) = g(d) [\psi_{vol}(\mathbf{b}_e) + \psi_{iso}(\mathbf{b}_e)] \quad \text{with} \quad \psi_{vol} = \frac{\kappa}{4}(I_3 - 1 - \ln I_3) \quad \text{and} \quad \psi_{iso} = \frac{\mu}{2}(I_3^{-1/3} I_1 - 3), \quad (16)$$

in terms of the bulk modulus $\kappa > 0$, the shear modulus $\mu > 0$, and the invariants: $I_1 = \text{tr } \mathbf{b}_e$ and $I_3 = \det \mathbf{b}_e$. The plastic contribution is assumed to have the form

$$W_{plas}(\alpha, d) = g(d) \psi_p(\alpha) \quad \text{with} \quad \psi_p = Y_0 \alpha + \frac{H}{2} \alpha^2 + (Y_{\infty} - Y_0)(\alpha + \exp[-\delta \alpha]/\delta), \quad (17)$$

with the initial yield stress Y_0 , infinite yield stress $Y_{\infty} \geq Y_0$, the isotropic hardening modulus $H \geq 0$, and the saturation parameter δ .

The degradation function $g(d) = (1-d)^2$ models the degradation of the elastic-plastic energy of the solid due to fracture. It interpolates between the unbroken response for $d = 0$ and the fully broken state at $d = 1$ by satisfying the constraints $g(0) = 1$, $g(1) = 0$, $g'(d) \leq 0$, and $g'(1) = 0$.

In order to enforce a crack evolution only in tension, the *volumetric* elastic energy is additively decomposed into a positive part ψ_{vol}^+ due to tension and a negative part ψ_{vol}^- due to compression, outlined in the pioneering work of Amor et al. (2009) as

$$W_{elas}(\mathbf{b}_e, d) = g(d) [\psi_{vol}^+(\mathbf{b}_e) + \psi_{iso}(\mathbf{b}_e)] + \psi_{vol}^-(\mathbf{b}_e) \quad \text{with} \quad \psi_{vol}^{\pm} = \frac{\kappa}{4}(I_3^{\pm} - 1 - \ln I_3^{\pm}), \quad (18)$$

in terms of the positive I_3^+ and the negative I_3^- third invariant defined as

$$\begin{aligned} I_3^+ &:= \max\{I_3, 1\} = \langle I_3 - 1 \rangle_+ + 1 = \frac{1}{2} \left[(I_3 - 1) + |I_3 - 1| \right] + 1 \\ I_3^- &:= \min\{I_3, 1\} = \langle I_3 - 1 \rangle_- + 1 = \frac{1}{2} \left[(I_3 - 1) - |I_3 - 1| \right] + 1, \end{aligned} \quad (19)$$

as visualized in Fig. 3. Following the Coleman-Noll procedure, the Kirchhoff stresses tensor $\boldsymbol{\tau}$ and the first Piola-Kirchhoff stress tensor \mathbf{P} are obtained from the elastic strain energy function $W_{elas}(\mathbf{b}_e, d)$ in Eq. (18) for isotropic material behavior as

$$\boldsymbol{\tau} = 2\mathbf{b}_e \frac{\partial W_{elas}}{\partial \mathbf{b}_e} \quad \text{and} \quad \mathbf{P} = \boldsymbol{\tau} \mathbf{F}^{-T}. \quad (20)$$

The fracture part of pseudo-energy density (15) takes the form

$$W_{frac}(\mathcal{H}, d, \nabla d) = 2 \frac{\psi_c}{\zeta} l \gamma_l(d, \nabla d) + \frac{\eta_f}{2 \Delta t} (d - d_n)^2 + g(d) \mathcal{H}, \quad (21)$$

where $\Delta t := t - t_n > 0$ denotes the time step, $\psi_c > 0$ is a critical fracture energy, and ζ controls the post-critical range after crack initialization. Following the recent works of Aldakheel (2016) and Miehe et al. (2016a,b), the history field \mathcal{H} is defined by

$$\mathcal{H} := \max_{s \in [0, t]} D(\mathbf{b}_e, \alpha; s) \geq 0 \quad \text{with} \quad D := \left\langle \psi_{vol}^+ + \psi_{iso} + \psi_p - \psi_c \right\rangle_+ \quad (22)$$

with the Macaulay bracket $\langle x \rangle_+ := (x + |x|)/2$, that ensures the irreversibility of the crack evolution.

The finite elasto-plastic model requires additionally the formulation of a yield function, a hardening law, and an evolution equation for the plastic variables. The yield function restricts the elastic region. By assuming J_2 -plasticity with nonlinear isotropic hardening, the yield function has the form

$$\chi = \sqrt{3/2} |\mathbf{f}^p| - r^p \quad \text{with} \quad \mathbf{f}^p := \text{dev}[\boldsymbol{\tau}] = \boldsymbol{\tau} - \frac{1}{3} \text{tr}[\boldsymbol{\tau}] \mathbf{1} \quad \text{and} \quad r^p := \partial_\alpha W_{plas}, \quad (23)$$

in terms of the deviatoric plastic driving force \mathbf{f}^p and the resistance force r^p . With the yield function at hand, we define the dual dissipation function for visco-plasticity according to Perzyna-type model as

$$\Phi^*(\mathbf{f}^p, r^p) = \frac{1}{2\eta_p} \left\langle \sqrt{3/2} |\mathbf{f}^p| - r^p \right\rangle_+^2, \quad (24)$$

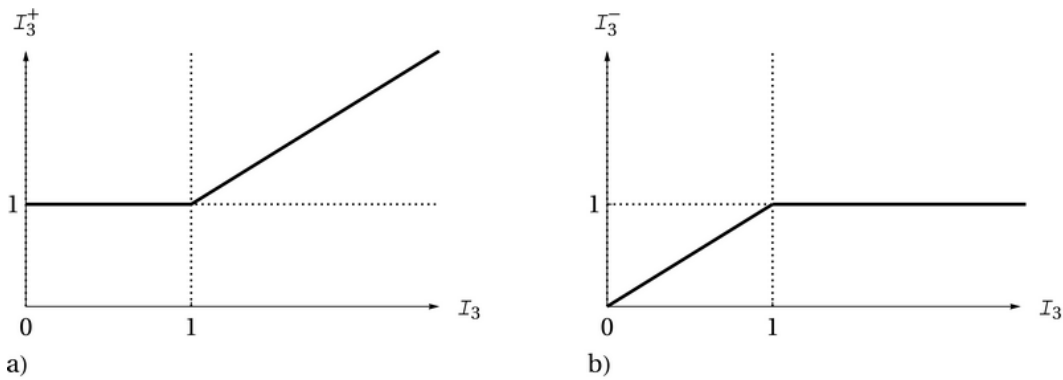


FIG. 3: Third invariant decomposition. (a) Positive part defined as $I_3^+ := \max\{I_3, 1\}$ and (b) negative part defined as $I_3^- := \min\{I_3, 1\}$.

with η_p being the viscosity parameter of the rate-dependent plastic deformation. The evolution equations for the plastic variables are (Hackl, 1997; Simo and Miehe, 1992; Wriggers, 2008; Wriggers and Hudobivnik, 2017)

$$-\frac{1}{2}\mathcal{L}_v \mathbf{b}_e = \dot{\gamma} \mathbf{n} \mathbf{b}_e \quad \text{with} \quad \mathbf{n} = \frac{\partial \chi}{\partial \mathbf{f}^p} \quad \text{and} \quad \dot{\alpha} = \dot{\gamma} := \frac{1}{\eta_p} \langle \chi \rangle_+, \quad (25)$$

where \mathcal{L}_v denotes the Lie derivative in time. The evolution equation (25)₁ can be recast with Eq. (5) in an alternative form

$$\dot{\mathbf{C}}_p^{-1} = -2\dot{\gamma} \mathbf{F}^{-1} \mathbf{n} \mathbf{F} \mathbf{C}_p^{-1}, \quad (26)$$

which will be used later for the algorithmic treatment of plasticity within the numerical solution algorithm (Korelc and Stupkiewicz, 2014). The Kuhn-Tucker conditions for the elasto-plastic model are

$$\chi \leq 0, \quad \dot{\gamma} \geq 0, \quad \text{and} \quad \chi \dot{\gamma} = 0. \quad (27)$$

The development of the virtual element formulation for the phase-field ductile fracture in elastic-plastic solids can start from a pseudo-potential density functional instead of using the weak form. This has advantages when the code is automatically generated using the software tool ACEGEN (Korelc and Wriggers, 2016). The pseudo-potential density functional depends on the elastic and the fracture parts and *keeps* the plastic history variables and the crack driving force *constant* during the first variation. The pseudo-potential density functional can then be written as

$$\Pi(\mathfrak{U}, \mathbf{h}) = \int_{\Omega} W(\mathfrak{C}) dV - \Pi_{ext}(\boldsymbol{\varphi}) \quad \text{with} \quad \Pi_{ext}(\boldsymbol{\varphi}) := \int_{\Omega} \bar{\mathbf{f}} \cdot \boldsymbol{\varphi} dV + \int_{\partial\Omega_t} \bar{\mathbf{t}} \cdot \boldsymbol{\varphi} dA. \quad (28)$$

Here $\mathbf{h} := \{\mathbf{C}_p^{-1}, \alpha, \mathcal{H}\}$ is the history field array for the plastic strain measures and the crack driving force.

3. FORMULATION OF THE VIRTUAL ELEMENT METHOD

Following the work of Brezzi et al. (2009), the main idea of the virtual element method is a Galerkin projection of the unknowns onto a specific ansatz space. The domain Ω is partitioned into non-overlapping polygonal elements which need not to be convex and can have any arbitrary shape with different node numbers, as plotted in Fig. 4 representing

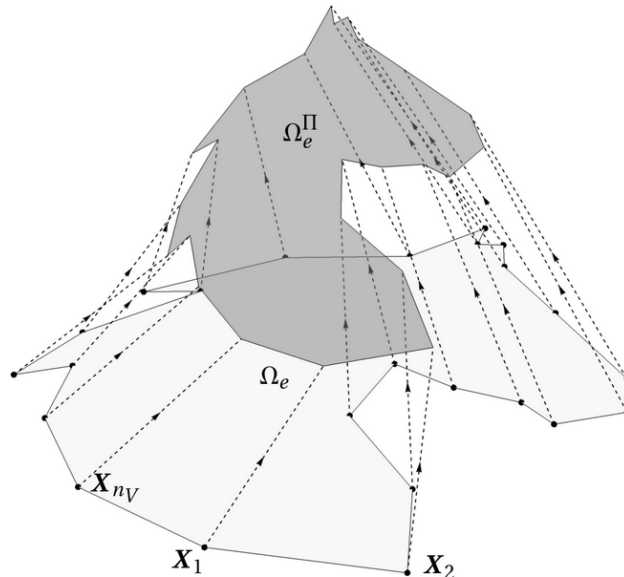


FIG. 4: Polynomial basis function for the virtual element ansatz with vertices \mathbf{X}_I

a *horse-like* element with X_I vertices. Here a low-order approach is adopted (Wriggers and Hudobivnik, 2017; Wriggers et al., 2017), using linear ansatz functions where nodes are placed only at the vertices of the polygonal elements. Furthermore, the restriction of the element shape functions to the element boundaries are linear functions.

3.1 Ansatz Functions for VEM

The VEM relies on the split of the ansatz space into a part \mathfrak{U}_Π representing the projected primary field defined in Eq. (13) and a remainder

$$\mathfrak{U}^h = \mathfrak{U}_\Pi^h + (\mathfrak{U}^h - \mathfrak{U}_\Pi^h) \quad \text{with} \quad \mathfrak{U}_\Pi^h := \{\varphi_\Pi^h, d_\Pi^h\}. \quad (29)$$

The projection \mathfrak{U}_Π^h is defined at element level by a linear ansatz function \mathbf{N}_Π as

$$\mathfrak{U}_\Pi^h = \begin{bmatrix} \varphi_{\Pi X} \\ \varphi_{\Pi Y} \\ d_\Pi \end{bmatrix} = \mathbf{a} \cdot \mathbf{N}_\Pi = \begin{bmatrix} a_1 & a_4 & a_7 \\ a_2 & a_5 & a_8 \\ a_3 & a_6 & a_9 \end{bmatrix} \begin{bmatrix} 1 \\ X \\ Y \end{bmatrix}, \quad (30)$$

with the unknowns \mathbf{a} . The projection \mathfrak{U}_Π^h is now defined such that it satisfies

$$\int_{\Omega_e} \nabla \mathfrak{U}_\Pi^h dV \stackrel{!}{=} \int_{\Omega_e} \text{Grad } \mathfrak{U}^h dV, \quad (31)$$

which yields, with the linear ansatz in Eq. (30) that $\nabla \mathfrak{U}_\Pi^h$ is constant as

$$\nabla \mathfrak{U}_\Pi^h|_e \stackrel{!}{=} \frac{1}{\Omega_e} \int_{\Omega_e} \text{Grad } \mathfrak{U}^h dV = \frac{1}{\Omega_e} \int_{\partial\Omega_e} \mathfrak{U}^h \otimes \mathbf{N} dA, \quad (32)$$

where \mathbf{N} is the normal at the boundary $\partial\Omega_e$ of the domain Ω_e of a virtual element e , see Fig. 5. Thus label $\square|_e$ represents element quantities that have constant value within an element e . A direct computation of the projected gradient yields with the linear ansatz in Eq. (30) the simple matrix form

$$\nabla \mathfrak{U}_\Pi^h|_e = \begin{bmatrix} \nabla \varphi_{\Pi X} \\ \nabla \varphi_{\Pi Y} \\ \nabla d_\Pi \end{bmatrix} = \begin{bmatrix} \varphi_{\Pi X,X} & \varphi_{\Pi X,Y} \\ \varphi_{\Pi Y,X} & \varphi_{\Pi Y,Y} \\ d_{\Pi,X} & d_{\Pi,Y} \end{bmatrix} = \begin{bmatrix} a_4 & a_7 \\ a_5 & a_8 \\ a_6 & a_9 \end{bmatrix}. \quad (33)$$

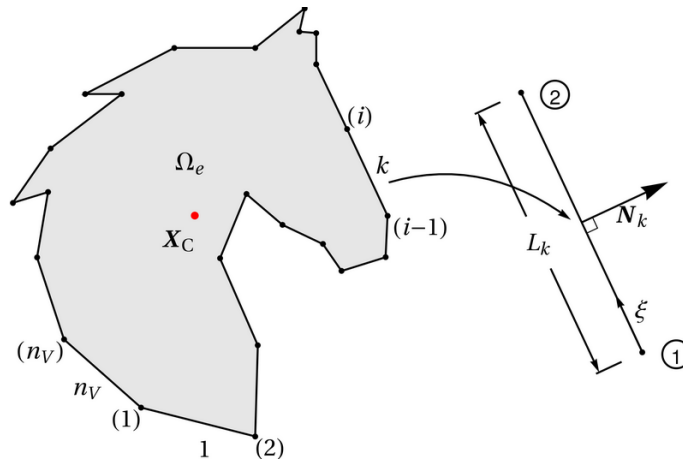


FIG. 5: Virtual element with n_V nodes and local boundary segment of the horse-like polygonal element

The boundary integral in Eq. (32) has to be evaluated. To this end, a linear ansatz for the primary fields along the element edges is introduced as

$$(\mathbf{u}^h)_k = (1 - \xi_k) \mathbf{u}_1 + \xi_k \mathbf{u}_2 = M_{k1} \mathbf{u}_1 + M_{k2} \mathbf{u}_2 \quad \text{with } \xi_k \in [0, 1], \quad (34)$$

for a boundary segment k of the virtual element. The local nodes: ①–② are chosen in counter-clockwise order and can be found in Fig. 5. In Eq. (34) M_{k1} is the ansatz function along a segment k , related to node ①, ξ_k is the local dimensionless coordinate, and \mathbf{u}_1 is the nodal value at that node. The ansatz function M_{k2} is defined in the same way. From Eqs. (32)–(34), the unknowns a_4 – a_9 can be computed from the normal vectors of the boundary segments in elements and the nodal primary fields as

$$\begin{bmatrix} a_4 & a_7 \\ a_5 & a_8 \\ a_6 & a_9 \end{bmatrix} = \frac{1}{\Omega_e} \int_{\partial\Omega_e} \mathbf{u}^h \otimes \mathbf{N} \, dA = \frac{1}{\Omega_e} \sum_{k=1}^{n_V} \int_{\partial\Omega_k} \begin{bmatrix} \varphi_X(\mathbf{X}) N_X & \varphi_X(\mathbf{X}) N_Y \\ \varphi_Y(\mathbf{X}) N_X & \varphi_Y(\mathbf{X}) N_Y \\ d(\mathbf{X}) N_X & d(\mathbf{X}) N_Y \end{bmatrix} dA, \quad (35)$$

where we have used $\mathbf{N} = \{N_X, N_Y\}^T$ and $\mathbf{u} = \{\varphi_X, \varphi_Y, d\}^T$, furthermore n_V is the number of element vertices which coincides with the number of segments (edges) of the element, for first-order VEM. Note that the normal vector \mathbf{N} changes from segment to segment. In the 2D case it can be computed for a segment k as

$$\mathbf{N}_k = \begin{Bmatrix} N_X \\ N_Y \end{Bmatrix}_k = \frac{1}{L_k} \begin{Bmatrix} Y_1 - Y_2 \\ X_2 - X_1 \end{Bmatrix}_k, \quad (36)$$

with $\{X_i, Y_i\}_{i=1,2}$ being the local coordinates of the two vertices of the segment k . The integral in Eq. (35) can be evaluated for the ansatz functions (34) exactly by using the trapezoidal or Gauss-Lobatto rule. By selecting the vertices as the Gauss-Lobatto points it is sufficient to know only the nodal values

$$\mathbf{u}_e = \{\mathbf{u}_1, \mathbf{u}_2, \dots, \mathbf{u}_{n_V}\} \quad (37)$$

at the n_V vertices V in Fig. 5. Since the ansatz function in Eq. (34) fulfills the property $M_I(X_J) = \delta_{IJ}$, the actual form of the function M does not enter the evaluation of the boundary integrals, which makes the evaluation extremely simple. Finally, by comparing (33) and (35) the unknowns a_4 to a_9 are obtained by inspection, for further details (Wriggers et al., 2017). The projection in Eq. (32) does not determine the ansatz \mathbf{u}_{Π}^h in Eq. (30) completely and has to be supplemented by a further condition to obtain the constants a_1 , a_2 , and a_3 . For this purpose we adopt the condition that the sum of the nodal values of \mathbf{u}^h and of its projection \mathbf{u}_{Π}^h are equal. This yields for each element Ω_e

$$\frac{1}{n_V} \sum_{I=1}^{n_V} \mathbf{u}_{\Pi}^h(\mathbf{X}_I) = \frac{1}{n_V} \sum_{I=1}^{n_V} \mathbf{u}^h(\mathbf{X}_I), \quad (38)$$

where \mathbf{X}_I are the coordinates of the nodal point I and the sum includes all boundary nodes. Substituting (30) and (34) in Eq. (38), results with the three unknowns a_1 , a_2 , and a_3 as

$$\begin{bmatrix} a_1 \\ a_2 \\ a_3 \end{bmatrix} = \frac{1}{n_V} \sum_{I=1}^{n_V} [\mathbf{u}_I - \nabla \mathbf{u}_{\Pi I} \cdot \mathbf{X}_I] = \frac{1}{n_V} \sum_{I=1}^{n_V} \begin{bmatrix} \varphi_{XI} - \varphi_{\Pi X, X} X_I - \varphi_{\Pi X, Y} Y_I \\ \varphi_{YI} - \varphi_{\Pi Y, X} X_I - \varphi_{\Pi Y, Y} Y_I \\ d_I - d_{\Pi, X} X_I - d_{\Pi, Y} Y_I \end{bmatrix}. \quad (39)$$

Thus, the ansatz function \mathbf{u}_{Π}^h of the virtual element is completely defined.

3.2 Construction of the Virtual Element

The VEM relies on the projection \mathbf{u}_{Π}^h of the deformation map and fracture phase field. This was approximated in the last section by a first-order polynomial leading to a gradient which has a constant value. This is called the consistency

term, but it does not lead to a stable formulation once the number of vertices is greater than 3. Thus the formulation has to be stabilized like the classical one-point integrated elements developed by Belytschko and Bindeman (1991), Flanagan and Belytschko (1981), Korelc et al. (2010), Krysl (2015b), Mueller-Hoeppe et al. (2009), Reese et al. (1999), and Reese and Wriggers (2000).

In the following development of the virtual element for the phase-field modeling of ductile fracture, the plastic variables and the crack driving force are computed from the consistency term. These variables are then used as given and fixed history values in the stabilization procedure.

To this end, the potential density functional defined in Eq. (28) can be rewritten by exploiting the split in Eq. (29). Thus we have, by summing up all element contributions for the n_e virtual elements

$$\Pi(\mathbf{u}, \mathbf{h}) = \bigwedge_{e=1}^{n_e} \Pi(\mathbf{u}_e, \mathbf{h}_e) \quad \text{with} \quad \Pi(\mathbf{u}_e, \mathbf{h}_e) = [\Pi_c(\mathbf{u}_\Pi^h, \mathbf{h})|_e + \Pi_{stab}(\mathbf{u}^h - \mathbf{u}_\Pi^h, \mathbf{h})|_e], \quad (40)$$

based on a constant part Π_c and an associated stabilization term Π_{stab} . Here the history fields array \mathbf{h}_e are local variables evaluated *only once* at the element level and used in both parts of the potential density functional. A summary of the algorithmic treatment for the finite strain plasticity and the crack driving force is outlined in Box 1, for further details we refer to the work of Wriggers and Hudobivnik (2017). The first part in Eq. (40)₂ can be computed as

$$\Pi_c^\tau(\mathbf{u}_\Pi^h, \mathbf{h})|_e = \int_{\Omega_e} W(\mathbf{e}_\Pi^h) dV - \int_{\Omega_e} \bar{\mathbf{f}} \cdot \boldsymbol{\varphi}_\Pi^h dV - \int_{\partial\Omega_e} \bar{\mathbf{t}} \cdot \boldsymbol{\varphi}_\Pi^h dA \quad \text{with} \quad \mathbf{e}_\Pi^h = \{\mathbf{b}_{e\Pi}^h, \alpha, \mathcal{H}, d_\Pi^h, \nabla d_\Pi^h\}. \quad (41)$$

The projected elastic left Cauchy-Green tensor $\mathbf{b}_{e\Pi}^h$ can be computed from the projected deformation map and the plastic part of the right Cauchy-Green tensor as

$$\mathbf{b}_{e\Pi}^h = \mathbf{F}_\Pi^h \mathbf{C}_p^{-1} \mathbf{F}_\Pi^{hT} \quad \text{with} \quad \mathbf{F}_\Pi^h = \nabla \boldsymbol{\varphi}_\Pi^h. \quad (42)$$

The primary fields \mathbf{u}_Π^h are linear functions and their gradient $\nabla \mathbf{u}_\Pi^h$ is constant over the area of the virtual element Ω_e , as a consequence, the pseudo-energy density per unit volume W is integrated by evaluating the function at the element centroid \mathbf{X}_c as shown in Fig. 5 and multiplying it with domain size Ω_e analogous to the standard Gauss integration scheme in FEM

Box 1: Algorithmic treatment of the history field array for the plastic strain measures and the crack driving force

Given: $\mathbf{F}_\Pi^h, d_\Pi, \mathbf{C}_{pn}^{-1}, \alpha_n, \mathcal{H}_n$	Find: $\mathbf{C}_p^{-1}, \alpha, \mathcal{H}$
$\mathbf{b}_{e\Pi}^h = \mathbf{F}_\Pi^h \mathbf{C}_{pn}^{-1} \mathbf{F}_\Pi^{hT}$	
$W_{elas}(\mathbf{b}_{e\Pi}^h, d_\Pi) = g(d_\Pi) [\psi_{vol}^+(\mathbf{b}_{e\Pi}^h) + \psi_{iso}(\mathbf{b}_{e\Pi}^h)] + \psi_{vol}^-(\mathbf{b}_{e\Pi}^h)$	
$W_{plas}(\alpha, d_\Pi) = g(d_\Pi) \psi_p(\alpha)$	
$\mathbf{f}^p := \text{dev}[\boldsymbol{\tau}] \quad \text{with} \quad \boldsymbol{\tau} = 2 \mathbf{b}_{e\Pi}^h \frac{\partial W_{elas}}{\partial \mathbf{b}_{e\Pi}^h}$	
$r^p = \partial_\alpha W_{plas}(\alpha, d_\Pi)$	
$\chi(\mathbf{f}^p, r^p) = \sqrt{3/2} \mathbf{f}^p - r^p$	
$\mathbf{C}_p^{-1} = \mathbf{F}_\Pi^{h-1} \exp \left[-2(\alpha - \alpha_n) \sqrt{3/2} \frac{\mathbf{f}^p}{ \mathbf{f}^p } \right] \mathbf{F}_\Pi^h \mathbf{C}_{pn}^{-1}$	
$\alpha = \alpha_n + \Delta\gamma$	
$\Delta\gamma = \frac{\Delta t}{\eta_p} \left\langle \chi(\mathbf{f}^p, r^p) \right\rangle_+ \geq 0$	
$\mathcal{H} := \max D(\mathbf{b}_{e\Pi}^h, \alpha) \geq 0 \quad \text{with} \quad D := \left\langle \psi_{vol}^+ + \psi_{iso} + \psi_p - \psi_c \right\rangle_+$	

$$\int_{\Omega_e} W(\mathfrak{C}_{\Pi}^h) dV = W(\mathfrak{C}_{\Pi}^h)|_c \Omega_e, \quad (43)$$

where the label $\square|_c$ refers to quantities evaluated at the element centroid \mathbf{X}_c . The pseudo potential is still a non-linear function with respect to the deformation map and the crack phase-field nodal degrees of freedom and the history field array.

Next, the stabilization potential has to be derived for the coupled problem based on the potential (28). Following the recent work of Wriggers et al. (2017), we introduce a non-linear stabilization procedure that takes the form

$$\Pi_{stab}(\mathfrak{U}^h - \mathfrak{U}_{\Pi}^h, \mathbf{h})|_e = \hat{\Pi}(\mathfrak{U}^h, \mathbf{h})|_e - \hat{\Pi}(\mathfrak{U}_{\Pi}^h, \mathbf{h})|_e. \quad (44)$$

For the stabilization density function \widehat{W} , we propose a similar function to the original density function (28), however scaled by a constant value β as: $\widehat{W} = \beta W$. In Eq. (44), the stabilization with respect to the projected primary fields $\hat{\Pi}^{\tau}(\mathfrak{U}_{\Pi}^h, \mathbf{h})|_e$ can then be calculated as Eq. (43), yielding

$$\hat{\Pi}(\mathfrak{U}_{\Pi}^h, \mathbf{h})|_e = \beta W(\mathfrak{C}_{\Pi}^h)|_c \Omega_e, \quad (45)$$

whereas the potential $\hat{\Pi}(\mathfrak{U}^h, \mathbf{h})|_e$ is computed by applying standard finite element method (FEM) procedure, i.e., by first discretizing the virtual element domain Ω_e into internal triangle element mesh consisting of $n_T = n_E - 2$ triangles as plotted in Fig. 6 for the *horse-like* polygonal element. Then the integral over Ω_e is transformed into the sum of integrals over triangles. By using a linear ansatz for the primary fields \mathfrak{U} , an approximation can be computed for the constitutive variables \mathfrak{C} within each triangle Ω_m^i of the inscribed mesh (Wriggers et al., 2017). This gives

$$\hat{\Pi}(\mathfrak{U}^h, \mathbf{h})|_e = \int_{\Omega_e} \widehat{W}(\mathfrak{C}^h) dV = \beta \int_{\Omega_e} W(\mathfrak{C}^h) dV = \beta \sum_i^{n_T} \Omega_e^i W(\mathfrak{C}^h)|_c, \quad (46)$$

where $W(\mathfrak{C}^h)|_c$ is the potential density function evaluated at the triangle centroid \mathbf{X}_c^i and Ω_e^i is the area of the i th triangle in the element e , as plotted in Fig. 6.

To compute the stabilization parameter β , a connection to the bending problem was imposed regarding the bulk energy as outlined in Wriggers and Hudobivnik (2017). By limiting the element size Ω_e toward 0, the difference between the potentials of projected values $\hat{\Pi}(\mathfrak{U}_{\Pi}^h, \mathbf{h})$ and the true values $\hat{\Pi}(\mathfrak{U}^h, \mathbf{h})$ will also approach toward 0, thus stabilization will disappear in limit. Due to the finer mesh requirements of the fracture phase-field problem compared

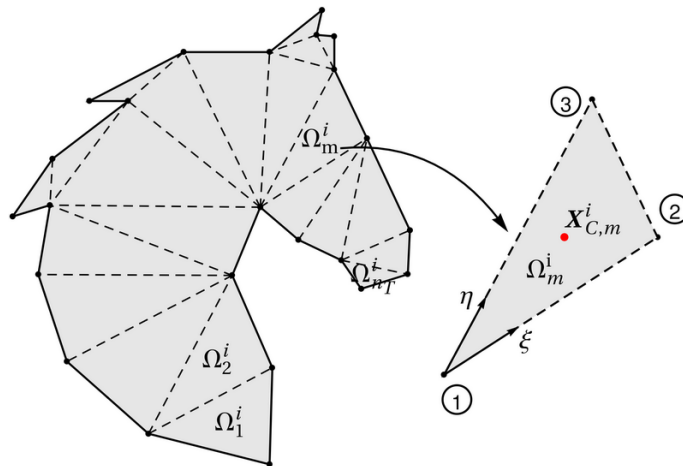


FIG. 6: Internal triangular mesh of the horse-like polygonal element

with Wriggers and Hudobivnik (2017), the choice of β factor term is less relevant, since it is only relevant for coarse meshes. In this regard we propose a constant value for β taken from the interval:

$$0 < \beta \leq 1. \quad (47)$$

Note that for β approaching zero, the potential $\Pi(\mathbf{u}^h, \mathbf{h})$ in Eq. (40) will depend only on the projection part $\Pi_c(\mathbf{u}_\Pi^h, \mathbf{h})$, leading to rank deficiency. However, when $\beta = 1$ the FEM results related to the internal mesh will be reproduced. Following our previous work on VEM for phase-field brittle fracture Aldakheel et al. (2018a), we chose a value for the stabilization parameter *at fracture* as $\beta = 0.4$ in all the simulations in Section 4, in which VEM coincide with FEM results. In case of a *pure elastic-plastic state*, the stabilization parameter follows the same procedure introduced in our previous works Aldakheel et al. (2019) and Hudobivnik et al. (2019) and takes the form

$$\beta = \min \left\{ 0.4, \frac{\sigma_{VM}}{E \alpha} \right\}, \quad (48)$$

where $\sigma_{VM} = \sqrt{3/2} |\mathbf{f}^p|$ is the von Mises stress, E is the Young's modulus, and α is the equivalent plastic strain providing an approximation for the tangent of the hardening curve.

All further derivations leading to the residual vector \mathbf{R}_e and the tangent matrix \mathbf{K}_e of the virtual element were performed with the software tool ACEGEN. This yields for Eq. (40) along with the potentials (41) and (44)–(46) the following:

$$\mathbf{R}_e = \frac{\partial \Pi(\mathbf{u}_e, \mathbf{h}_e)}{\partial \mathbf{u}_e} \quad \text{and} \quad \mathbf{K}_e = \frac{\partial \mathbf{R}_e}{\partial \mathbf{u}_e}, \quad (49)$$

where the history variables are treated as fixed fields in Eq. (49)₁, i.e., $\partial_{\mathbf{u}_e} \mathbf{h}_e = 0$. With these expressions at hand, we adopt a global Newton-Raphson algorithm for the coupled problem, resulting in the following linearized system:

$$\mathbf{R} + \mathbf{K} \Delta \mathbf{u} = 0 \quad \text{with} \quad \mathbf{R} = \bigwedge_{e=1}^{n_e} \mathbf{R}_e, \quad \mathbf{K} = \bigwedge_{e=1}^{n_e} \mathbf{K}_e \quad \text{and} \quad \mathbf{u} = \bigwedge_{e=1}^{n_e} \mathbf{u}_e, \quad (50)$$

that determines at given global primary fields \mathbf{u} their linear increment $\Delta \mathbf{u}$ in a typical Newton-type iterative solution step. This system of non-linear equations has to be solved in a nested algorithm, where the deformation map and the crack phase field are the global unknown variables.

4. REPRESENTATIVE NUMERICAL EXAMPLES

We now demonstrate the performance of the proposed virtual element formulation for the phase-field modeling of ductile fracture at finite deformations by means of two representative numerical examples. For comparison purposes, results of the standard FEM are also demonstrated. All computations are performed by using a nested Newton-Raphson algorithm. Load stepping is applied when necessary. Because all formulations are linearized in a consistent manner using ACEGEN, quadratic convergence is achieved within a load step. The material parameters used in this section are the same for all examples and given in Table 1. They are used by many authors in the literature as a reference for metals (Hallquist, 1984; Simo, 1988). In Section 4.1, we compare VEM and FEM results for the standard single-edge-notched shear test of Aldakheel (2016), Ambati et al. (2015), and Miehe et al. (2017). Finally, an axial stretch of a bar is investigated in Section 4.2.

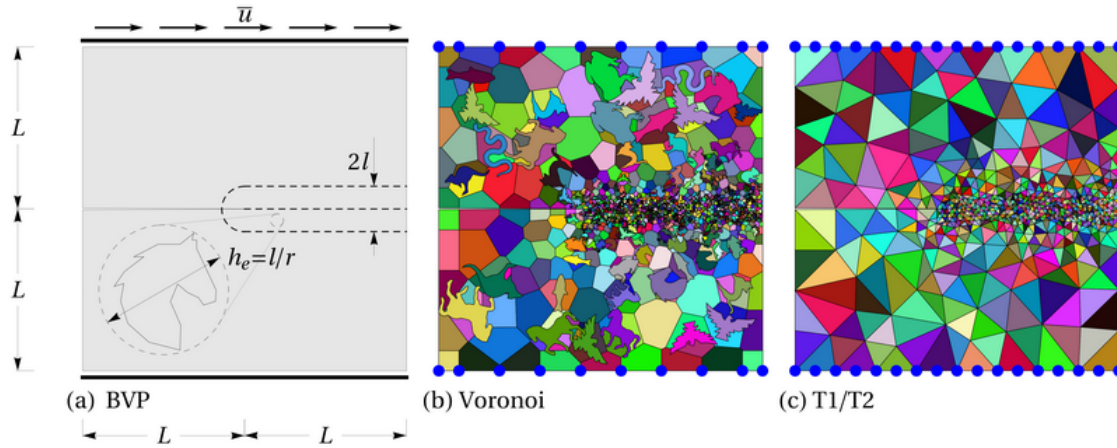
To illustrate the capability and the flexible choice of the number of nodes in an element for VEM, various animal-shaped Voronoi cells (bird, horse, snake, frog, koala, fish, kangaroo, ...) are employed in the undamaged as well as the damaged zones (i.e., an area of interest) for the virtual element formulation in the following sections.

4.1 Single-Edge Notched Shear Test

The first benchmark test considers a square plate with a horizontal notch placed at the middle height from the left outer surface to the center of the specimen. The geometrical setup and the loading conditions of the specimen are

TABLE 1: Material parameters used in the numerical examples

No.	Parameter	Name	Value	Unit
1.	E	Young's modulus	206.9	GPa
2.	ν	Poisson's ratio	0.29	—
3.	H	Hardening parameter	0.13	GPa
4.	Y_0	Initial yield stress	0.45	GPa
5.	Y_∞	Infinite yield stress	0.45/1.165	GPa
6.	δ	Saturation parameter	16.93	—
7.	ψ_c	Critical fracture energy	0.025/2.0	GPa
8.	η_p	Plastic viscosity	10^{-8}	GPa.s
9.	η_f	Fracture viscosity	10^{-8}	GPa.s
10.	l	Fracture length scale	0.008/0.02	mm
11.	ζ	Fracture parameter	8.0/1.0	—

**FIG. 7:** Single-edge notched shear test. (a) Geometry and boundary conditions, (b) VEM with Voronoi mesh, and (c) triangular finite element mesh.

depicted in Fig. 7(a). The size of the square specimen is chosen to be $L = 0.5$ mm. We fixed the bottom edge of the plate and applied shear loading to the top edge until the plate is fully broken. The specimen is discretized by using different virtual elements in Fig. 7(b) and finite element formulations in Fig. 7(c). Here we use the following notations: VEM-VO with a Voronoi mesh; VEM-T2 with 6 noded triangle representing a *first-order* VEM (Note that: T2 in this case implies that the triangle mesh used is the same as for the second-order FEM and *not second-order VEM*); FEM-T1 with linear triangle, and FEM-T2 with quadratic triangle, to test the robustness of the virtual element formulation. A mesh refinement in the expected fracture zone is applied, this is based on the ratio $r := l/h_e$ between the mesh size h_e and the fracture length scale l , as sketched in Fig. 7(a).

The evolution of the crack phase field d in comparison to the evolution of the equivalent plastic strain α for three different deformation stages up to final rupture are depicted in Fig. 8. This was achieved by using the virtual element formulations with various animal-shaped Voronoi cells, for fracture length scale $l = 0.008$ mm and the length/mesh ratio $r = 4$. The crack phase field initiates at the notch-tip, see Fig. 8(e), where the maximum equivalent plastic strain α is concentrated as shown in Fig. 8(a). Thereafter, the crack propagates horizontally till separation in Fig. 8(g), as outlined in Aldakheel (2016), Ambati et al. (2015), and Miehe et al. (2017).

Load-displacement curves of the overall structural response are plotted for different elements formulations of FEM and VEM for comparison purposes in Fig. 9(a). The VEM results are in a good agreement with the reference works. Table 2 compares the different FEM and VEM discretization, related to F-U curves in Fig. 9(a), with respect to robustness and efficiency. Figure 9(b) illustrates the convergence properties for the different element formulations

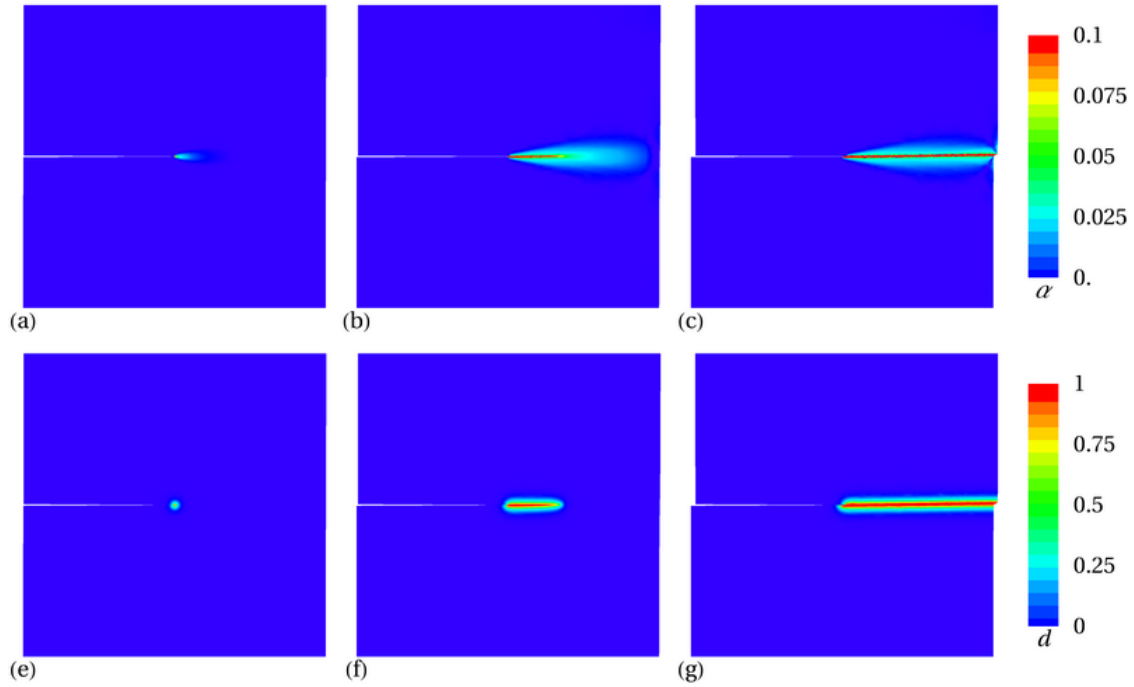


FIG. 8: Single-edge notched shear test. Contour plots of the equivalent plastic strain α in (a)–(c) and the fracture phase-field d in (e)–(g) for three different deformation states up to final rupture.

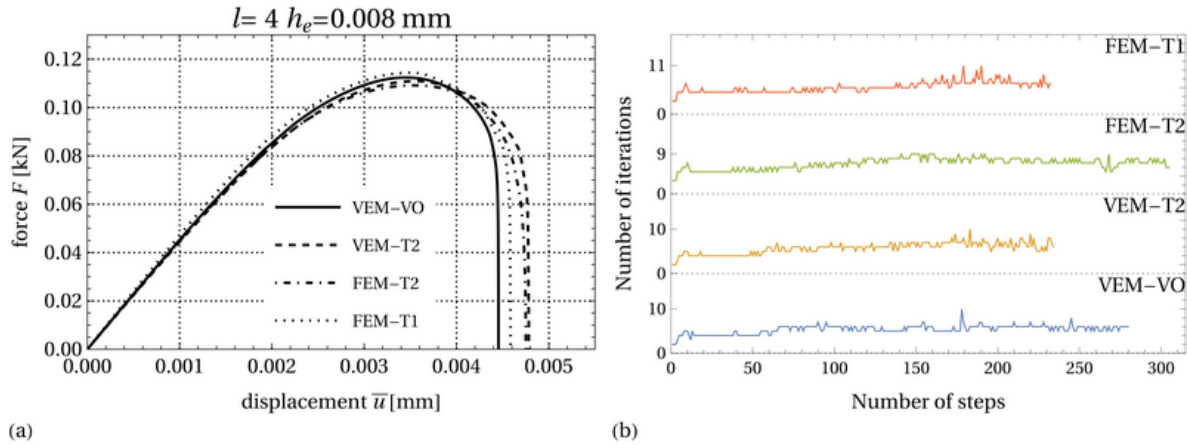


FIG. 9: Single-edge notched shear test. (a) Load–displacement responses for different VEM and FEM discretization. (b) Comparison between the total number of iterations in each time step that required to achieve convergence for different discretization.

plotted in Fig. 9(a) at the final deformation state $\bar{u} = 0.0048$ mm. We observe that virtual elements required *fewer* steps and iterations for final convergence compared with FEM of higher order. Thus here, VEM is more robust than FEM, however, this comes with extra computational costs.

4.2 Axial Stretch of a Bar

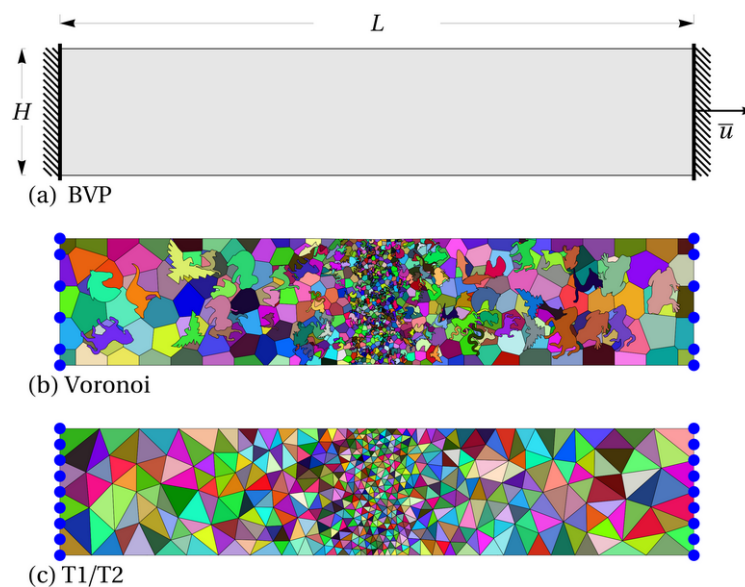
The second numerical example is concerned with analyzing the ductile failure behavior of a bar due to a prescribed displacement \bar{u} along the axial direction at the right side. It is a standard benchmark problem of finite plasticity and has

TABLE 2: A comparison between different FEM and VEM discretizations, related to F-U curves in Fig. 9(a)

	VEM-VO	VEM-T2	FEM-T2	FEM-T1
Number of elements	12,369	11,109	11,109	11,109
Number of nodes	24,744	22,291	22,290	5,591
Number of equations	74,195	66,826	66,826	16,749
Number of steps	280	234	305	232
Total number of iterations	2,372	1,504	2,610	1,599
Average iterations/step	6.1134	5.76245	6.97861	6.07985

been analyzed by many authors (Aldakheel, 2017; Aldakheel and Miehe, 2017; Miehe et al., 2014; Simo and Miehe, 1992). Experimental observation shows that a necking zone takes place before final ductile rupture. The localized plastic strains in the necking area and the subsequent ductile failure response will be used to test the robustness of the virtual element formulation. The geometrical setup and the boundary conditions of the bar with height $H = 2$ mm and length $L = 10$ mm are illustrated in Fig. 10. To trigger localization and necking in the center of the bar, a geometrical imperfection is introduced in the central zone. Here, a reduction of the specimen net section at the central zone is applied, in which the height at the center is chosen to be $H_c = 0.99 H$. At the left edge of the bar we applied a Dirichlet boundary condition of $\bar{u} = 0$ and applied a horizontal displacement at the right edge that has the magnitude of 20% of the bar length, e.g., $\bar{u} = 0.2L$. A mesh refinement in the expected fracture zone is applied for all VEM and FEM element formulations, see Figs. 10(b) and 10(c).

Figure 11 shows the contour plots of the equivalent plastic strain α and the fracture phase field d simulated using the virtual element formulations with various animal-shaped Voronoi cells, for fracture length scale $l = 0.02$ mm and different deformation stages up to final failure. We observed a huge plastic deformation as a necking zone with concentration hardening in Figs. 11(b) and 10(c) at the specimen center, resulting with crack initiation at center zone as demonstrated in Fig. 11(i). Thereafter, the crack phase field propagates outward following the equivalent plastic strain path till the complete failure as shown in Figs. 11(j) and 10(k). Load-displacement curves for different elements formulations of FEM and VEM are displayed in Fig. 12. All simulations show similar behavior before crack

**FIG. 10:** Axial stretch of a bar. (a) Geometry and boundary conditions, (b) VEM with Voronoi mesh, and (c) triangular finite element mesh.

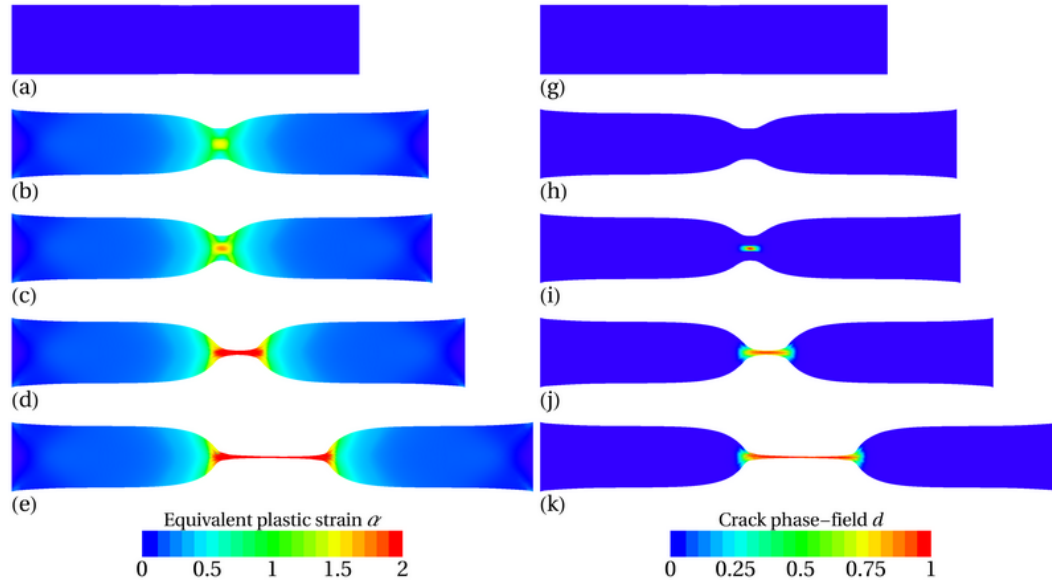


FIG. 11: Axial stretch of a bar. Contour plots of the equivalent plastic strain α in (a)–(e) and the fracture phase-field d in (g)–(k) for five different deformation states up to final rupture.

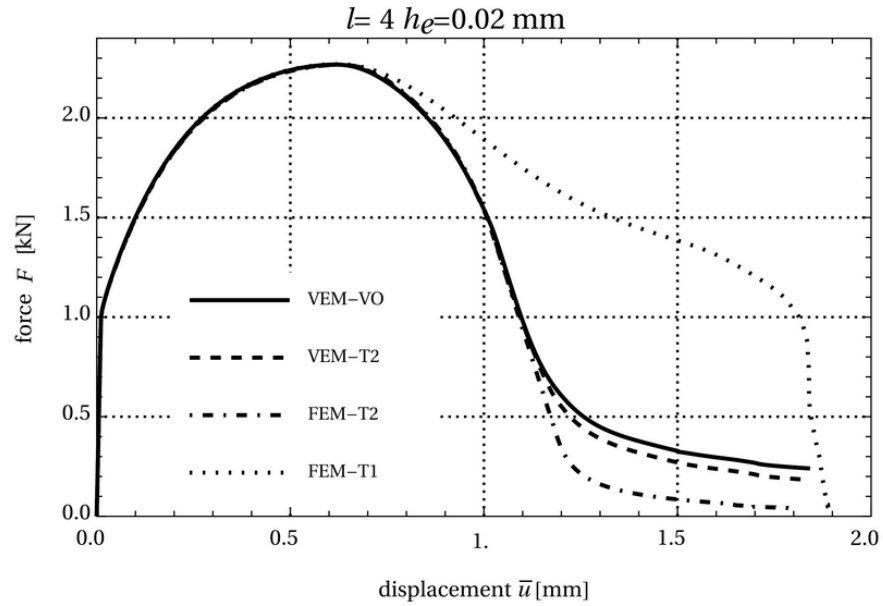


FIG. 12: Axial stretch of a bar. Load–displacement responses for different VEM and FEM discretization

initiation. Thereafter, all elements show almost closer results, except the FEM–T1 which exhibit a stiffer response. As a consequence, the capability of VEM element with Voronoi mesh is comparable to using finite elements of higher order.

5. CONCLUSION

A virtual element scheme for the phase-field modeling of isotropic ductile fracture was outlined within this work. It represents an initial contribution to the use of the VEM for numerically solving fracture-mechanics problems. In contrast to the projection of the deformation map field as the only global field being sought in most virtual element method applications up to now, this work further extends VEM toward multi-physics problems. To this end, we proposed a minimization of a pseudo-potential density functional for the coupled problem undergoing large strains. The key aspect of development was the extension toward the virtual element formulation due to its flexibility in dealing with complex element shapes that can even be non convex and arbitrary number of nodes. We examined the performance of the formulation by means of two numerical examples.

ACKNOWLEDGMENTS

This paper is dedicated to the memory of the late Professor Christian Miehe (1956–2016). The corresponding author gratefully acknowledges support for this research by the “German Research Foundation” (DFG) in (i) the COLLABORATIVE RESEARCH CENTER CRC 1153 “Process chain for the production of hybrid high-performance components through tailored forming,” (ii) the PRIORITY PROGRAM SPP 2020 under the project WR 19/58-1, and (iii) the PRIORITY PROGRAM SPP 1748 under the project WR 19/50-1.

REFERENCES

- Aldakheel, F., *Mechanics of Nonlocal Dissipative Solids: Gradient Plasticity and Phase Field Modeling of Ductile Fracture*, PhD, Institute of Applied Mechanics (CE), Chair I, University of Stuttgart, 2016. DOI: 10.18419/opus-8803
- Aldakheel, F., Micromorphic Approach for Gradient-Extended Thermo-Elastic-Plastic Solids in the Logarithmic Strain Space, *Continuum Mech. Thermodynam.*, vol. **29**, no. 6, pp. 1207–1217, 2017.
- Aldakheel, F., Hudobivnik, B., and Wriggers, P., Virtual Elements for Finite Thermo-Plasticity Problems, *Comput. Mech.*, 2019. DOI: 10.1007/s00466-019-01714-2
- Aldakheel, F., Hudobivnik, B., Hussein, A., and Wriggers, P., Phase-Field Modeling of Brittle Fracture Using an Efficient Virtual Element Scheme, *Comput. Methods Appl. Mech. Eng.*, vol. **341**, pp. 443–466, 2018a.
- Aldakheel, F., Kienle, D., Keip, M.A., and Miehe, C., Phase Field Modeling of Ductile Fracture in Soil Mechanics, *Proc. Appl. Math. Mech.*, vol. **17**, no. 1, pp. 383–384, 2017.
- Aldakheel, F., Mauthe, S., and Miehe, C., Towards Phase Field Modeling of Ductile Fracture in Gradient-Extended Elastic-Plastic Solids, *Proc. Appl. Math. Mech.*, vol. **14**, pp. 411–412, 2014.
- Aldakheel, F. and Miehe, C., Coupled Thermomechanical Response of Gradient Plasticity, *Int. J. Plasticity*, vol. **91**, pp. 1–24, 2017.
- Aldakheel, F., Wriggers, P., and Miehe, C., A Modified Gurson-Type Plasticity Model at Finite Strains: Formulation, Numerical Analysis and Phase-Field Coupling, *Comput. Mech.*, vol. **62**, no. 4, pp. 815–833, 2018b.
- Alessi, R., Ambati, M., Gerasimov, T., Vidoli, S., and De Lorenzis, L., Comparison of Phase-Field Models of Fracture Coupled with Plasticity, in *Advances in Computational Plasticity*, Springer International Publishing, pp. 1–21, 2018a.
- Alessi, R., Vidoli, S., and De Lorenzis, L., A Phenomenological Approach to Fatigue with a Variational Phase-Field Model: The One-Dimensional Case, *Eng. Fracture Mech.*, vol. **190**, no. 1, pp. 53–73, 2018b.
- Ambati, M., Gerasimov, T., and De Lorenzis, L., Phase-Field Modeling of Ductile Fracture, *Comput. Mech.*, vol. **55**, pp. 1017–1040, 2015.
- Amor, H., Marigo, J., and Maurini, C., Regularized Formulation of the Variational Brittle Fracture with Unilateral Contact: Numerical Experiments, *J. Mech. Phys. Solids*, vol. **57**, pp. 1209–1229, 2009.
- Artioli, E., Beirão da Veiga, L., Lovadina, C., and Sacco, E., Arbitrary Order 2D Virtual Elements for Polygonal Meshes: Part I, Elastic Problem, *Comput. Mech.*, vol. **60**, no. 3, pp. 355–377, 2017.
- Bathe, K.J., *Finite Element Procedures*, Englewood Cliffs, NJ: Prentice-Hall, 1996.
- Beirão Da Veiga, L., Brezzi, F., Cangiani, A., Manzini, G., Marini, L.D., and Russo, A., Basic Principles of Virtual Element Methods, *Math. Models Methods Appl. Sci.*, vol. **23**, no. 1, pp. 199–214, 2013a.

- Beirão Da Veiga, L., Brezzi, F., and Marini, L.D., Virtual Elements for Linear Elasticity Problems, *SIAM J. Numer. Anal.*, vol. **51**, no. 2, pp. 794–812, 2013b.
- Bellis, M.L.D., Wriggers, P., Hudobivnik, B., and Zavarise, G., Virtual Element Formulation for Isotropic Damage, *Finite Elements Anal. Des.*, vol. **144**, pp. 38–48, 2018.
- Belytschko, T. and Bindeman, L.P., Assumed Strain Stabilization of the 4-Node Quadrilateral with 1-Point Quadrature for Non-linear Problems, *Comput. Methods Appl. Mech. Eng.*, vol. **88**, no. 3, pp. 311–340, 1991.
- Bleyer, J. and Alessi, R., Phase-Field Modeling of Anisotropic Brittle Fracture Including Several Damage Mechanisms, *Comput. Methods Appl. Mech. Eng.*, vol. **336**, no. 1, pp. 213–236, 2018.
- Boerner, E., Loehnert, S., and Wriggers, P., A New Finite Element based on the Theory of a Cosserat Point—Extension to Initially Distorted Elements for 2D Plane Strain, *Int. J. Numer. Methods Eng.*, vol. **71**, pp. 454–472, 2007.
- Böger, L., Keip, M.A., and Miehe, C., Minimization and Saddle-Point Principles for the Phase-Field Modeling of Fracture in Hydrogels, *Comput. Mater. Sci.*, vol. **138**, pp. 474–485, 2017.
- Borden, M.J., Hughes, T.J., Landis, C.M., Anvari, A., and Lee, I.J., A Phase-Field Formulation for Fracture in Ductile Materials: Finite Deformation Balance Law Derivation, Plastic Degradation, and Stress Triaxiality Effects, *Comput. Methods Appl. Mech. Eng.*, vol. **312**, pp. 130–166, 2016.
- Borden, M.J., Verhoosel, C.V., Scott, M.A., Hughes, T.J.R., and Landis, C.M., A Phase-Field Description of Dynamic Brittle Fracture, *Comput. Methods Appl. Mech. Eng.*, vols. **217–220**, pp. 77–95, 2012.
- Brezzi, F., Buffa, A., and Lipnikov, K., Mimetic Finite Differences for Elliptic Problems, *ESAIM: Math. Model. Numer. Anal.*, vol. **43**, no. 2, pp. 277–295, 2009.
- Cangiani, A., Manzini, G., Russo, A., and Sukumar, N., Hourglass Stabilization and the Virtual Element Method, *Int. J. Numer. Methods Eng.*, vol. **102**, nos. 3–4, pp. 404–436, 2015.
- Chi, H., Beirão da Veiga, L., and Paulino, G., Some Basic Formulations of the Virtual Element Method (VEM) for Finite Deformations, *Comput. Methods Appl. Mech. Eng.*, vol. **318**, pp. 148–192, 2017.
- Choo, J. and Sun, W., Coupled Phase-Field and Plasticity Modeling of Geological Materials: From Brittle Fracture to Ductile Flow, *Comput. Methods Appl. Mech. Eng.*, vol. **330**, pp. 1–32, 2018.
- Dittmann, M., Aldakheel, F., Schulte, J., Wriggers, P., and Hesch, C., Variational Phase-Field Formulation of Non-Linear Ductile Fracture, *Comput. Methods Appl. Mech. Eng.*, vol. **342**, pp. 71–94, 2018.
- Dittmann, M., Hesch, C., Schulte, J., Aldakheel, F., and Franke, M., Multi-Field Modelling and Simulation of Large Deformation Ductile Fracture, *Proc. of the XIV International Conference on Computational Plasticity. Fundamentals and Applications*, Barcelona, Spain, pp. 556–567, 2017.
- Dittmann, M., Krüger, M., Schmidt, F., Schuß, S., and Hesch, C., Variational Modeling of Thermomechanical Fracture and Anisotropic Frictional Mortar Contact Problems with Adhesion, *Comput. Mech.*, vol. **63**, no. 3, pp. 571–591, 2019.
- Duda, F.P., Ciarbonetti, A., Sánchez, P.J., and Huespe, A.E., A Phase-Field/Gradient Damage Model for Brittle Fracture in Elastic-Plastic Solids, *Int. J. Plasticity*, vol. **65**, pp. 269–296, 2014.
- Ehlers, W. and Luo, C., A Phase-Field Approach Embedded in the Theory of Porous Media for the Description of Dynamic Hydraulic Fracturing, *Comput. Methods Appl. Mech. Eng.*, vol. **315**, pp. 348–368, 2017.
- Flanagan, D. and Belytschko, T., A Uniform Strain Hexahedron and Quadrilateral with Orthogonal Hour-Glass Control, *Int. J. Numer. Methods Eng.*, vol. **17**, pp. 679–706, 1981.
- Gain, A.L., Talischi, C., and Paulino, G.H., On the Virtual Element Method for Three-Dimensional Linear Elasticity Problems on Arbitrary Polyhedral Meshes, *Comput. Methods Appl. Mech. Eng.*, vol. **282**, pp. 132–160, 2014.
- Gültekin, O., Dal, H., and Holzapfel, G.A., A Phase-Field Approach to Model Fracture of Arterial Walls: Theory and Finite Element Analysis, *Comput. Methods Appl. Mech. Eng.*, vol. **312**, pp. 542–566, 2016.
- Hackl, K., Generalized Standard Media and Variational Principles in Classical and Finite Strain Elastoplasticity, *J. Mech. Phys. Solids*, vol. **45**, no. 5, pp. 667–688, 1997.
- Hallquist, J.O., Nike 2D: An Implicit, Finite Deformation, Finite Element Code for Analyzing the Static and Dynamic Response of Two-Dimensional Solids, Lawrence Livermore National Laboratory, University of California, Livermore, CA, Rep. UCRL-52678, 1984.
- Heider, Y. and Markert, B., A Phase-Field Modeling Approach of Hydraulic Fracture in Saturated Porous Media, *Mech. Res. Commun.*, vol. **80**, pp. 38–46, 2017.

- Hesch, C., Franke, M., Dittmann, M., and Temizer, I., Hierarchical NURBS and a Higher-Order Phase-Field Approach to Fracture for Finite-Deformation Contact Problems, *Comput. Methods Appl. Mech. Eng.*, vol. **301**, pp. 242–258, 2016.
- Hesch, C. and Weinberg, K., Thermodynamically Consistent Algorithms for a Finite-Deformation Phase-Field Approach to Fracture, *Int. J. Numer. Methods Eng.*, vol. **99**, pp. 906–924, 2014.
- Hudobivnik, B., Aldakheel, F., and Wriggers, P., A Low Order 3D Virtual Element Formulation for Finite Elasto-Plastic Deformations, *Comput. Mech.*, vol. **63**, no. 2, pp. 253–269, 2019.
- Korelc, J., Solinc, U., and Wriggers, P., An Improved EAS Brick Element for Finite Deformation, *Comput. Mech.*, vol. **46**, pp. 641–659, 2010.
- Korelc, J. and Stupkiewicz, S., Closed-Form Matrix Exponential and Its Application in Finite-Strain Plasticity, *Int. J. Numer. Methods Eng.*, vol. **98**, pp. 960–987, 2014.
- Korelc, J. and Wriggers, P., *Automation of Finite Element Methods*, Switzerland: Springer, 2016.
- Krysl, P., Mean-Strain Eight-Node Hexahedron with Optimized Energy-Sampling Stabilization for Large-Strain Deformation, *Int. J. Numer. Methods Eng.*, vol. **103**, pp. 650–670, 2015a.
- Krysl, P., Mean-Strain Eight-Node Hexahedron with Stabilization by Energy Sampling Stabilization, *Int. J. Numer. Methods Eng.*, vol. **103**, pp. 437–449, 2015b.
- Kuhn, C., Schlüter, A., and Müller, R., On Degradation Functions in Phase Field Fracture Models, *Comput. Mater. Sci.*, vol. **108**, pp. 374–384, 2015.
- Miehe, C., Aldakheel, F., and Raina, A., Phase Field Modeling of Ductile Fracture at Finite Strains. A Variational Gradient-Extended Plasticity-Damage Theory, *Int. J. Plasticity*, vol. **84**, pp. 1–32, 2016a.
- Miehe, C., Aldakheel, F., and Teichtmeister, S., Phase-Field Modeling of Ductile Fracture at Finite Strains: A Robust Variational-Based Numerical Implementation of a Gradient-Extended Theory by Micromorphic Regularization, *Int. J. Numer. Methods Eng.*, vol. **111**, no. 9, pp. 816–863, 2017.
- Miehe, C., Hofacker, M., Schänzel, L.M., and Aldakheel, F., Phase Field Modeling of Fracture in Multi-Physics Problems. Part II. Brittle-to-Ductile Failure Mode Transition and Crack Propagation in Thermo-Elastic-Plastic Solids, *Comput. Methods Appl. Mech. Eng.*, vol. **294**, pp. 486–522, 2015a.
- Miehe, C., Kienle, D., Aldakheel, F., and Teichtmeister, S., Phase Field Modeling of Fracture in Porous Plasticity: A Variational Gradient-Extended Eulerian Framework for the Macroscopic Analysis of Ductile Failure, *Comput. Methods Appl. Mech. Eng.*, vol. **312**, pp. 3–50, 2016b.
- Miehe, C., Schänzel, L., and Ulmer, H., Phase Field Modeling of Fracture in Multi-Physics Problems. Part I. Balance of Crack Surface and Failure Criteria for Brittle Crack Propagation in Thermo-Elastic Solids, *Comput. Methods Appl. Mech. Eng.*, vol. **294**, pp. 449–485, 2015b.
- Miehe, C., Teichtmeister, S., and Aldakheel, F., Phase-Field Modeling of Ductile Fracture: A Variational Gradient-Extended Plasticity-Damage Theory and Its Micromorphic Regularization, *Philos. Trans. R. Soc. A: Math., Phys. Eng. Sci.*, vol. **374**, no. 2066, 2016c.
- Miehe, C., Welschinger, F., and Aldakheel, F., Variational Gradient Plasticity at Finite Strains. Part II: Local-Global Updates and Mixed Finite Elements for Additive Plasticity in the Logarithmic Strain Space, *Comput. Methods Appl. Mech. Eng.*, vol. **268**, pp. 704–734, 2014.
- Miehe, C., Welschinger, F., and Hofacker, M., Thermodynamically Consistent Phase-Field Models of Fracture: Variational Principles and Multi-Field FE Implementations, *Int. J. Numer. Methods Eng.*, vol. **83**, pp. 1273–1311, 2010.
- Mueller-Hoeppel, D.S., Loehnert, S., and Wriggers, P., A Finite Deformation Brick Element with Inhomogeneous Mode Enhancement, *Int. J. Numer. Methods Eng.*, vol. **78**, pp. 1164–1187, 2009.
- Nadler, B. and Rubin, M., A New 3D Finite Element for Nonlinear Elasticity Using the Theory of a Cosserat Point, *Int. J. Solids Struct.*, vol. **40**, pp. 4585–4614, 2003.
- Reese, S., Kuessner, M., and Reddy, B.D., A New Stabilization Technique to Avoid Hourglassing in Finite Elasticity, *Int. J. Numer. Methods Eng.*, vol. **44**, pp. 1617–1652, 1999.
- Reese, S. and Wriggers, P., A New Stabilization Concept for Finite Elements in Large Deformation Problems, *Int. J. Numer. Methods Eng.*, vol. **48**, pp. 79–110, 2000.
- Reinoso, J., Paggi, M., and Linder, C., Phase Field Modeling of Brittle Fracture for Enhanced Assumed Strain Shells at Large Deformations: Formulation and Finite Element Implementation, *Comput. Mech.*, vol. **59**, no. 6, pp. 981–1001, 2017.

- Simo, J.C., A Framework for Finite Strain Elastoplasticity based on Maximum Plastic Dissipation and the Multiplicative Decomposition. Part II: Computational Aspects, *Comput. Methods Appl. Mech. Eng.*, vol. **68**, pp. 1–31, 1988.
- Simo, J.C. and Miehe, C., Associative Coupled Thermoplasticity at Finite Strains: Formulation, Numerical Analysis and Implementation, *Comput. Methods Appl. Mech. Eng.*, vol. **98**, pp. 41–104, 1992.
- Taylor, R.L. and Artioli, E., VEM for Inelastic Solids, *Adv. Comput. Plasticity. Comput. Methods Appl. Sci.*, vol. **46**, pp. 381–394, 2018.
- Teichtmeister, S., Kienle, D., Aldakheel, F., and Keip, M.A., Phase Field Modeling of Fracture in Anisotropic Brittle Solids, *Int. J. Non-Linear Mech.*, vol. **97**, pp. 1–21, 2017.
- Verhoosel, C.V. and de Borst, R., A Phase-Field Model for Cohesive Fracture, *Int. J. Numer. Methods Eng.*, vol. **96**, pp. 43–62, 2013.
- Wriggers, P., *Nonlinear Finite Elements*, Berlin: Springer, 2008.
- Wriggers, P. and Hudobivnik, B., A Low Order Virtual Element Formulation for Finite Elasto-Plastic Deformations, *Comput. Methods Appl. Mech. Eng.*, vol. **327**, pp. 459–477, 2017.
- Wriggers, P., Hudobivnik, B., and Korelc, J., *Efficient Low Order Virtual Elements for Anisotropic Materials at Finite Strains*, Cham, Switzerland: Springer International Publishing, pp. 417–434, 2018a.
- Wriggers, P., Hudobivnik, B., and Schröder, J., *Finite and Virtual Element Formulations for Large Strain Anisotropic Material with Inextensive Fibers*, Cham, Switzerland: Springer International Publishing, pp. 205–231, 2018b.
- Wriggers, P., Reddy, B.D., Rust, W., and Hudobivnik, B., Efficient Virtual Element Formulations for Compressible and Incompressible Finite Deformations, *Comput. Mech.*, vol. **60**, no. 2, pp. 253–268, 2017.
- Wriggers, P., Rust, W.T., and Reddy, B.D., A Virtual Element Method for Contact, *Comput. Mech.*, vol. **58**, no. 6, pp. 1039–1050, 2016.
- Zhang, X., Vignes, C., Sloan, S.W., and Sheng, D., Numerical Evaluation of the Phase-Field Model for Brittle Fracture with Emphasis on the Length Scale, *Comput. Mech.*, vol. **59**, no. 5, pp. 737–752, 2017.
- Zienkiewicz, O.C., Taylor, R., and Zhu, J.Z., *The Finite Element Method: Its Basis and Fundamentals*, Amsterdam: Elsevier, 2005.